Characterization of the photon detection system for the LHCb RICH upgrade

Maria Belen del Valle Coello

August 2019

1 Introduction

The LHCb experiment is a single arm spectrometer designed to perform precise measurements of heavy-flavour physics observables. In LHCb the hadron identification, and in particular the pions and kaons separation, is provided by two Ring Imaging Cherenkov (RICH) detectors: RICH 1 and RICH 2. Both RICH detectors provide Particle Identification (PID) measuring the Cherenkov radiation produced by charged particles traversing a volume of fluorocarbon gas used as radiator [1]. A schematic of LHCb is shown in Figure 1.

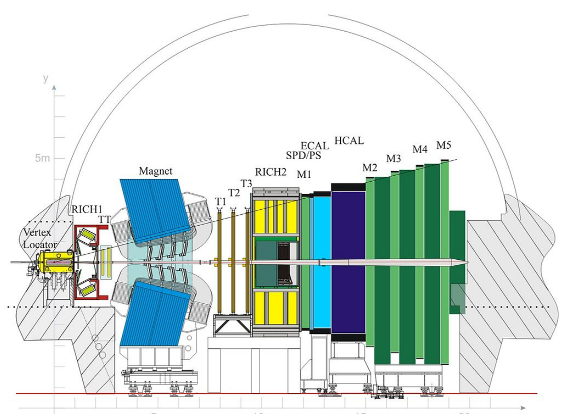

Figure 1: Schematic of the LHCb detector. Taken from [1].

During the second long shutdown LHCb is upgrading the whole experiment in order to run at a higher instantaneous luminosity ($2x10^{33}cm^{-2}s^{-1}$) and at higher readout rate (40 MHz), starting from 2021. In order to achieve this, the LHCb collaboration plans to remove first hardware trigger level which was limiting the data acquisition rate to 1 MHz, therefore all sub-detectors will need to upgrade their readout to cope with a significantly higher rate [1].

2 RICH Layout and MaPMTs

In order to be able to operate in the upgrade conditions, the whole optics and mechanics of RICH 1, the upstream RICH detector, has been redesigned. Moreover in both RICH 1 and RICH 2 the opto-electronics chain will be replaced since the former Hybrid Photon Detectors (HPD) were equipped with embedded front-end electronics. The photon detectors chosen for the RICH upgrade are Multi-anode Photomultiplier Tubes (MaPMTs), produced by Hamamatsu, with 64 anodes per MaPMT: the one inch R13742 (R-type) will be installed in RICH 1 and the central region of RICH 2 while the 2 inches R13743 (H-type) will be installed in the peripheral areas of RICH 2 [2]. A diagram of the front face of RICH2 is shown in Figure 2.

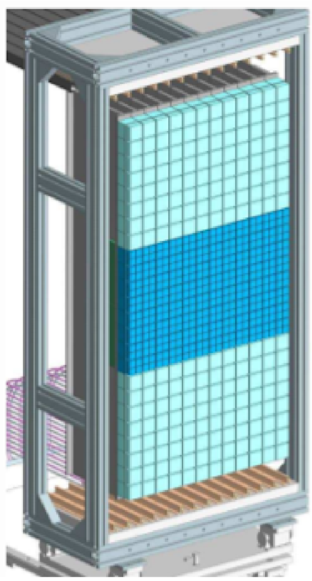

Figure 2: Schematic of the RICH 2 detector panels. The center is composed of R-type MaPMTs for higher granularity, while the outside has generally less occupancy and so is composed of H-type MaPMTs

3 Characterisation of the MaPMTs

During the past years an intense campaign, both in laboratory and on beam, has been conducted by the RICH collaboration in order to fully characterise MaPMTs. One of the features currently under study is the Signal Induced Noise (SIN), which manifests itself as noise occurring approximately 100 ns after the initial signal in the MaPMT and can persist for over 2 μs. Since its discovery in 2018, SIN has been extensively studied by the RICH group to evaluate its impact on the upgraded detectors. Among the observables studied so far, SIN has been investigated as a function of the MaPMT gain, the dark count rate, the high voltage, and several other parameters. The common characteristic found in every unit is the topology of SIN: it is confined to the top and bottom rows of the MaPMT (namely pixels 1-8 and 57-64), resulting in a level of noise which is an intrinsic characteristic of each unit.

3.1 Quantum Efficiency Measurements

One of the most important parameters for the characterization of any PMT is the quantum efficiency (QE), which is essentially the baseline, first-order probability for signal detection. To measure quantum efficiency, we assess for each incoming photon what percentage of these photons generates a photoelectron in the MaPMT that is then measured in the photocathode current. Additionally, though SIN has been studied extensively and is well-understood by the RICH collaboration, the relation between quantum efficiency and SIN levels in a photomultiplier had not been studied yet.

We decided to investigate the relation of SIN and QE in three MaPMTs. One of these, FA1265, had been measured to have a high degree of SIN, while the ZN1871 and ZN1874 were specially manufactured by Hamamatsu to have lower SIN [3]. FA0216 served as a reference MaPMT (Fig.3).

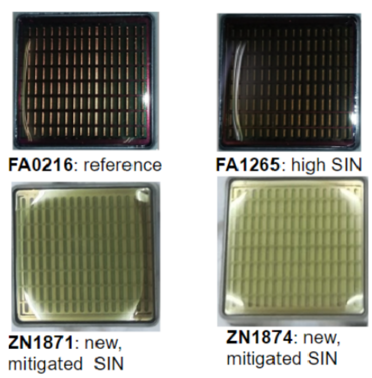

Figure 3: MaPMTs used in QE SIN tests. Each MaPMT has a different level of SIN from the others.

The measurement of quantum efficiency is both critical and difficult, and excellent stability of all the measurement apparatuses is necessary. The measurements were performed with the dedicated setup whose diagram is shown in Figure 4.

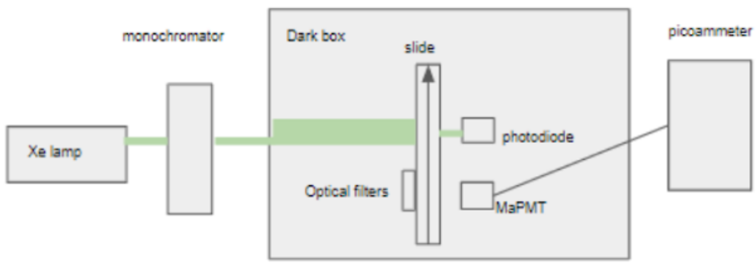

Figure 4: Schematic of quantum efficiency measurement setup. Wavelengths of interest from the xenon source are selected via the monochromator and passed into the darkbox. The light shines directly into the reference photodiode and is read out with the computer system. To test the MaPMTs, the slide is shifted and the optical filters and MaPMT are placed before the light source. The MaPMT is read out using a picoammeter.

The xenon lamp was first assessed for stability by running a wavelength scan from 200 to 700 nm incident on the reference photodiode. The first two runs were taken at the beginning of the quantum efficiency measurements and the last one after all the data had been taken. As shown in Figure 5, the lamp was highly stable and considered sufficient for our measurements of quantum efficiency.

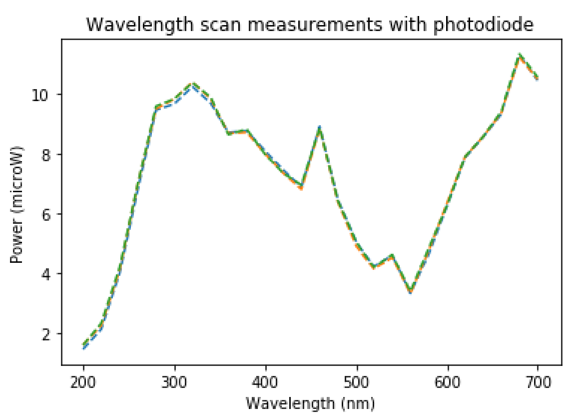

Figure 5: Plot of wavelength scan for lamp stability. Two of the scans were taken consecutively, and the last scan was taken around 20 minutes later. The lamp is highly stable.

The second step of this process was to measure the IV curve of the MaPMTs and hence find a voltage to bias the cathode at which the MaPMTs' response was constant. This was done by setting the monochromator to 320 nm (where the QE for these units is peaking) and then for each voltage applied acquire the photocathode current by means of a picoammeter. The IV curve is shown in Figure 6. Based on the results, we selected a value of -50 V applied on the photocathode as the operating voltage for the quantum efficiency measurements.

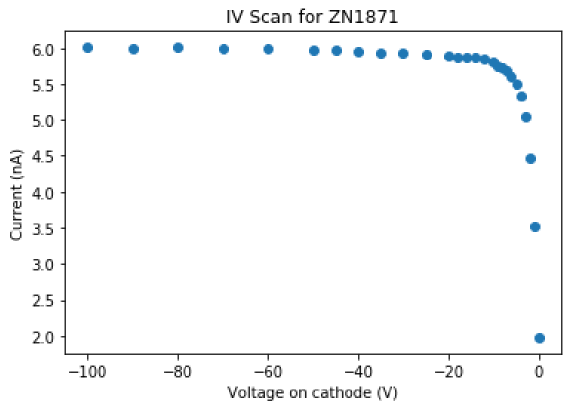

Figure 6: IV Curve for MaPMT ZN1871. At voltages greater in magnitude than -20V, the MaPMT has a plateau in its response; one can choose one of these higher voltages to measure quantum efficiency.

After establishing stability and calibrating the components, we were able to measure the quantum efficiency of the various MaPMTs. To do so, we performed a wavelength scan with the light incident on the MaPMT while the photocathode is biased at -50V and recorded the output current with the picoammeter. To check for background noise, we performed another wavelength scan without light incident on the MaPMT set to -50V.

The first measurement was performed on FA0216, whose QE had been measured multiple times over the past years [1]. The new QE curve was found to be compatible with previous measurements validating the reliability of the test setup. Then the other three units were measured and the results for each MaPMT are shown in Figure 7.

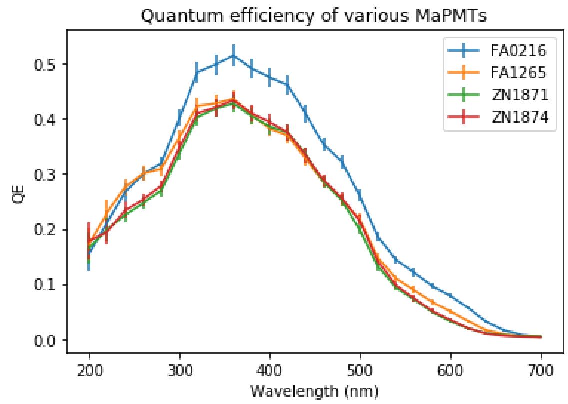

Figure 7: Quantum efficiency of the MaPMTs. FA0216 served as the reference.

As shown, the peak quantum efficiencies were similar for all of the MaPMTs we measured, only a small difference for wavelengths lower than 280nm is visible and it is due to a small difference in the photocathode material. Hence, we concluded that the SIN of an MaPMT has no measurable dependence on the quantum efficiency of the photomultiplier tube.

3.2 Measurement of SIN

SIN data acquisition mostly occurred at CERN, in the characterization and assembly laboratory for the RICH group. The setup was composed of 16 MaPMTs mounted on 4 Elementary Cells (EC) containing the upgrade front-end electronics and readout through 12 data links. A schematic of the elementary cell structure is shown in Figure 8, and a picture of the setup for measuring SIN is shown in Figure 9.

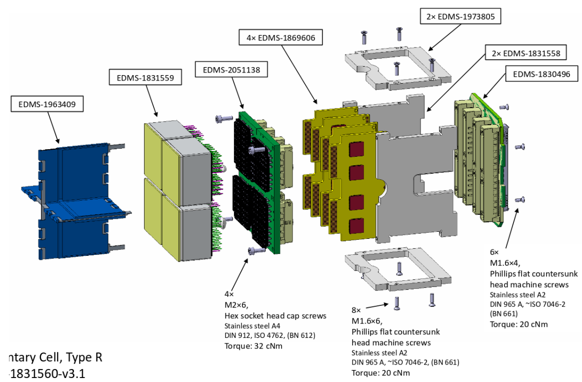

Figure 8: The R-type elementary cell, composed of 4 MaPMTs mounted on readout electronics.

Figure 9: The back side of the SIN measurement setup. The orange cables are plugged into the Teflon boards to provide uniform illumination from the laser onto the MaPMTs, which are mounted directly behind them.

The standard test procedure consisted of three runs of 23 million events each, in order to acquire a full signal peak, noise peak, and noise tail for each pixel of the MaPMT. These runs extend for approximately 1700 ns. The three runs are then merged into a single histogram which we then analyze. One such histogram is shown in Figure 10.

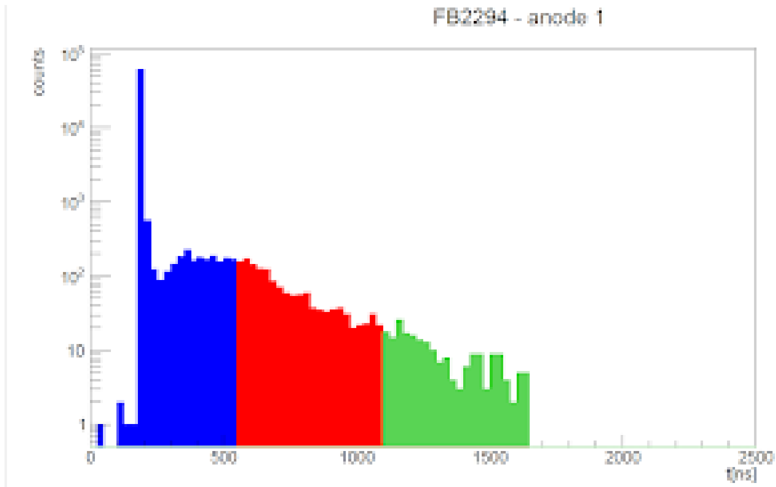

Figure 10: Example SIN distribution. The run shown in blue contains the signal peak and the noise peak, while the red and green runs show the tail of the SIN noise distribution.

3.3 Reducing SIN Data Volume with Peak-Determined Prediction

The RICH upgrade is reaching the final stage of testing in the laboratory before the new detector is installed underground. The ECs are assembled in columns equipped with the final cabling and services. The first test column, shown in Figure 11 has been built at the beginning of the summer and it is currently used to finalise the commissioning test plan.

Figure 11: First completed RICH 2 column used for testing this summer.

The data volume produced by the SIN measurements is acceptable for few MaPMT testing, but it becomes time-consuming and resource-intensive when applied to the entire column now, and then to the full detectors after the installation. Each column of RICH 2 will be equipped with 32 R-Type and 16 H-type MaPMTs reaout via 40 data links while each RICH 1 column will be equipped with 96 R-Type MaPMTs readout via 72 data links. Performing the standard set of runs to characterise the SIN on one column would correspond to a huge volume of data difficult to handle on a routine basis.

Our focus in this analysis is to find a way to cut down on this data volume and find a comprehensive way to describe SIN and predict its distribution in each PMT simply by acquiring one million events at the noise and signal peaks, reducing the data acquisition by a factor of 34.5.

The data is organized into a tree denoted by the elementary cell number, the photomultiplier number, and finally the pixel number, in which the histograms containing each run's data are stored. Using ROOT's TSpectrum class, we found the peak positions for the noise peak and the signal peak for all of the pixels, and wrote their positions in time and amplitude into a Python numpy array. The position of the "valley," or the lowest point between the signal and noise peaks, was also extracted from each histogram.

For the peak-finding algorithm, we had to specify the threshold with which a noise peak would be accepted as a percentage of the signal peak. After some initial configuring, the threshold value was chosen as 0.1 percent, as this value most accurately located the position of the noise peak. The result of few pixels' peak detection is shown in Figure 12. As one can see, the inner pixels are not highly affected by SIN, and the peak-finding does not locate any peaks there.

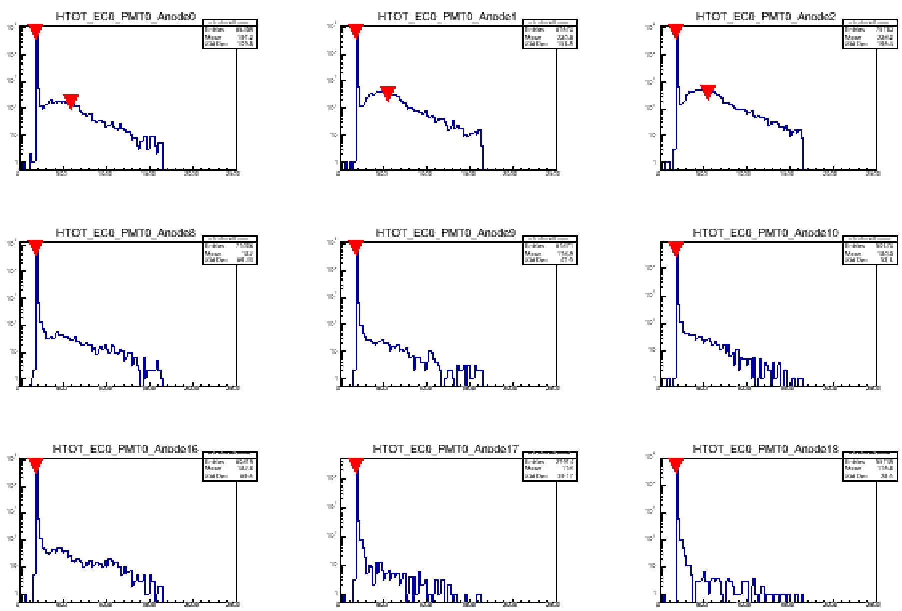

Figure 12: Example SIN peak finding for a subset of a single MaPMT's pixels. The noise peak of the SIN is found only in the edge pixels, as expected.

Having generated the peak and valley timing and amplitude information from all the pixels, we then selected only the information from the R-type elementary cells and the edge pixels for our initial analysis, so that we could construct a more accurate parameterization of the SIN. This is because the SIN hasn't been detected in H-type MaPMTs where any time delayed noise can be described as traditional afterpulsing.

Some initial histograms had to be made to understand the timing distribution of the signal and noise peak. The signal peak was extremely consistent, occurring at 187.5 ns for all MaPMTs. The noise peak was a little less consistent, with some spread around the mean value, as shown in Figure 13.

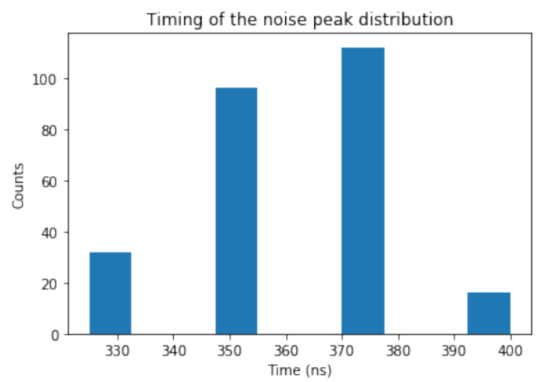

Figure 13: Timing of the noise peaks for R-Type MaPMTs tested. Overall, the noise peak occurs between 330 ns and 400 ns, which corresponds to around 150 to 210 ns delay between the signal and noise peaks.

One of the main goals for this analysis was to find a relation between the signal to noise ratio (SNR) using just the peaks of the SIN distribution and the SNR obtained by integrating the signal and noise separately. The expected linear relation between the two types of SNR would allow us to obtain data at only the two peak positions and then convert these into a signal and noise distribution automatically. For this, the extracted SNR was computed by taking the integral of the signal histogram up to the valley position, then taking the integral of the noise histogram from the valley position to the end position. The SN/SN plot generated from the peak-finding algorithm is shown in Figure 14.

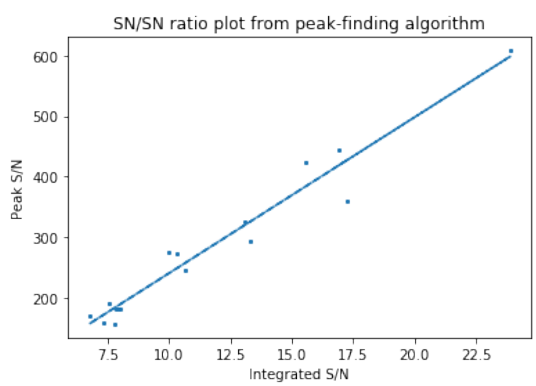

Figure 14: Ratio plot from peak finding algorithm. There is more scatter than we would like at high SN values. The data plotted is from elementary cells 0 through 3, corresponding to R-type MaPMTs.

After creating this plot, we noticed a significant dispersion from the expected linear relation between the two signal to noise ratios. Upon further investigation we observed some offsets between where the noise peaks in the pixels were visually observed and where the peak-finding algorithm found the peaks. Hence, we decided to test whether specifying where the peak should be observed would decrease the dispersion of the SN ratios plot. To do so, we made a histogram of the time position of the actual maximum value of the noise for each pixel, and then chose the mean of that distribution as the noise peak position. This yielded a SN ratio with much lower scatter, as shown in Figure 15.

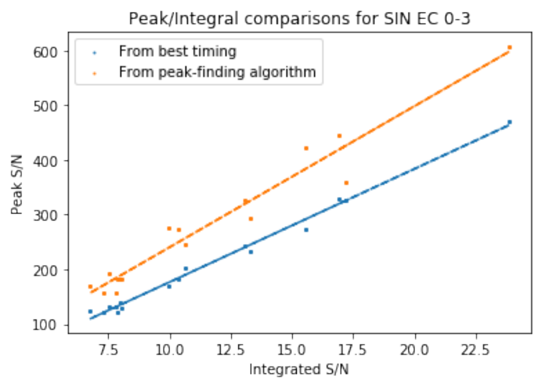

Figure 15: Comparison between the peak finding algorithm and the manual proper timing of the peak. Clearly, the manual timing yields less scatter around the linear relation of SN/SN.

This investigation yielded a linear relationship between the two extracted SN ratios and, based on the low-scatter linearity of the best-timing SNR to SNR plot, suggests a universal timing for SIN noise peaks. If shown to be consistent across all the columns that will be assembled and tested in the next few months, the algorithms generated in this project will be used to automatically generate the SIN distribution for all pixels of RICH's MaPMTs.

4 Acknowledgements

I would like to thank Silvia Gambetta and Thierry Gys for the opportunity to work on this project as a CERN Summer Student and for their support and advice on everything from physics to life. I would also like to thank Antonino Sergi and Giovanni Cavallero for their help in explaining the WINCC machine and their tireless work to reconfigure the machine so that we could run both the individual MaPMT and the assembled column tests that we needed. In general, many thanks to the excellent LHCb collaboration for bringing me on to such an interesting and exciting project!

5 References

[1] LHCb collaboration, *LHCb reoptimized detector design and performance: Technical Design Report*, CERN-LHCC-2003-030. LHCb-TDR-009.
[2] M. Fiorini. "The LHCb RICH Detector Upgrade." In PoS(EPS-HEP2017)494.
[3] Internal communications, Hamamatsu, 2018.